



Research papers

Improving evapotranspiration partitioning by integrating satellite vegetation parameters into a land surface model

Dawei Peng^{a,b}, Xianhong Xie^{a,b,*}, Shunlin Liang^c, Yibing Wang^{a,b}, Arken Tursun^{a,b}, Yao Liu^{a,b}, Kun Jia^{a,b}, Han Ma^c, Yuchao Chen^{a,b}

^a State Key Laboratory of Remote Sensing Science, Faculty of Geographical Science, Beijing Normal University, Beijing 100875, China

^b Beijing Engineering Research Center for Global Land Remote Sensing Products, Faculty of Geographical Science, Beijing Normal University, Beijing 100875, China

^c Jockey Club STEM Laboratory of Quantitative Remote Sensing, Department of Geography, University of Hong Kong, Hong Kong 999077, China

ARTICLE INFO

Keywords:

Evapotranspiration partitioning
Land surface model
Dynamic vegetation
Satellite vegetation, Leaf area index
Fraction of vegetation coverage

ABSTRACT

Land evapotranspiration (ET) primarily involves vegetation transpiration, canopy interception loss, and soil evaporation. Previous studies have made significant progress in total ET estimation; however, substantial challenges remain in partitioning ET on a regional scale, largely due to the intricate water and energy balance that is disrupted by vegetation cover changes. The accuracy of land surface models in representing ET components may be constrained by their inadequate consideration of vegetation dynamics. In this study, we integrate satellite leaf area index (LAI) and fraction of vegetation coverage (FVC) into the Variable Infiltration Capacity model (VIC) to improve ET partitioning ability in the Loess Plateau of China, a region that has experienced substantial vegetation dynamics. The results showed that satellite dynamic vegetation parameters in modeling are effective in improving the estimation of ET components compared with the default/static vegetation parameters. Considering LAI dynamics in the model enhances the representation of the inter- and intra-annual variations in vegetation transpiration and canopy interception loss. Dynamic FVC reasonably allocates transpiration to soil evaporation, capturing evaporation in forest gaps effectively. This effect is particularly relevant in arid and semi-arid regions. Among the ET components, transpiration was the most sensitive to the two dynamic vegetation parameters, followed by canopy interception loss and soil evaporation. Through the VIC model with dynamic vegetation parameters, our study revealed that soil evaporation was twice that of transpiration in the Loess Plateau, which is consistent with its semi-arid region and relatively sparse vegetation coverage. Our study offers valuable insights regarding the use of vegetation coverage for partitioning ET and highlights the advantage of integrating satellite vegetation products into land surface models.

1. Introduction

Evapotranspiration (ET) serves as a crucial nexus within the water, energy, and carbon cycles (Mianabadi et al. 2019; Wang et al. 2014; Yang et al. 2023; Zhou et al. 2016). ET can typically be partitioned into vegetation transpiration (Et), soil evaporation (Es), canopy interception loss (Ec), snow sublimation (Esn), and evaporation from open water. Excepting open water evaporation, these components are strongly influenced by vegetation dynamics (Good et al. 2017; Liu et al. 2020; Yang et al. 2023). Against the backdrop of global greening (Chen et al. 2019; Piao et al. 2020), changes in vegetation introduce substantial uncertainties into the accurate partitioning of ET (Cao et al. 2022; Li et al. 2020; Yang et al. 2023). Accurate ET components are essential for

agricultural water management and assessing ecological project benefits. Therefore, understanding the mechanisms of ET components is crucial in regions facing high water stress, ensuring food security, and maintaining ecological and environmental conditions (Mu et al. 2007; Song et al. 2018).

Previous studies have employed various technologies to estimate ET and its components, including remote sensing-based models, field experiments, and process-based land surface models. Regarding remote sensing-based models, while they cannot directly extract ET from satellite images, they can integrate satellite data (e.g., vegetation parameters and energy balance products) with physical or empirical formulas to estimate ET and its components (Mu et al. 2007; Tian et al. 2013; Zhang et al. 2019). Over the past several decades, such remote sensing-

* Corresponding author.

E-mail address: xianhong@bnu.edu.cn (X. Xie).

<https://doi.org/10.1016/j.jhydrol.2024.131928>

Received 23 June 2024; Received in revised form 8 August 2024; Accepted 24 August 2024

Available online 2 September 2024

0022-1694/© 2024 Elsevier B.V. All rights are reserved, including those for text and data mining, AI training, and similar technologies.

based models have been the primary approach for regional and global ET estimation because of the availability of various remote sensing products (Bastiaanssen et al. 1998a; Bastiaanssen et al. 1998b; Zhang et al. 2008). However, partitioning ET using remote sensing-based models remains challenging, partly because these models oversimplify physical processes, such as neglecting the contribution of water constraints during the evaporation process. (Lian et al., 2018; Miralles et al., 2016; Talsma et al., 2018b). Alternatively, in field experiments to estimate ET, models based on field-measured data have been proposed to estimate Et and other components (Duursma et al. 2013; Fisher et al. 2008; Jiao et al. 2018; Jiao et al. 2015; Jung et al. 2019; Sus et al. 2014). However, owing to the constraints imposed by various local conditions, field experiments often focus more on an individual ET component than on all components or the full water balance at a point scale (Schlesinger and Jasechko 2014; Zhang et al. 2023). For example, after using a global field experiment dataset to estimate Et, Gao et al. (2022) highlighted the importance to consider both biotic and abiotic factors when estimating other ET components. This undoubtedly poses greater challenges for experimental instruments and field conditions during monitoring.

Process-based land surface models, including the Variable Infiltration Capacity (VIC) model (Liang et al. 1994), Noah Multi-parameterization (Noah-MP) model (Chen et al. 1996), and Community Land Model (CLM) (Oleson et al. 2004), offer several advantages in estimating ET and its components (Ge et al. 2011; Yeh et al. 2011; Zhang et al. 2017). By coupling water and energy balances with biogeophysical processes to capture large-scale ET, these process-based models enable a deeper comprehension and explication of ET (Haddeland et al. 2006). Consequently, they have extensive applications at the regional and global scales (Jiang et al. 2022; Lawrence et al. 2007; Luo et al. 2016). Nevertheless, ET component estimation remains controversial owing to the inadequate consideration of vegetation dynamics during ET partitioning.

Process-based land surface models generally apply land cover information within a region to partition ET into biotic (e.g., Et and Ec) and abiotic (i.e., Es) components (Haddeland et al. 2006). The subsequent estimation of Et and Ec depends on vegetation structure dynamics, such as the leaf area index (LAI) (Liang et al. 1994; Yang et al. 2021). Process-based models are typically subject to the representation of vegetation conditions and generally adopt two approaches to address vegetation dynamics. The first approach couples a dynamic vegetation module to the CLM or Noah-MP (Hosseini et al. 2022; Jasechko et al. 2013; Lawrence et al. 2019; Sato et al. 2014), utilizing vegetation physiology and biophysical formulations to derive vegetation dynamics (Dickinson et al. 1998). The second approach integrates satellite vegetation parameters into a physical model, such as the VIC model, to capture the dynamic state of vegetation (Bohn and Vivoni 2016; Jiang et al. 2022; Meng et al. 2020; Xie et al. 2015). However, dynamic vegetation modeling remains characterized by substantial uncertainty because of the complexity of biophysical processes (Anav et al. 2013; Cadule et al. 2010; Shu et al. 2022; Sitch et al. 2015), whereas satellite products are reliable means for obtaining regional and global vegetation dynamics. Nevertheless, the extent to which satellite dynamic vegetation parameters can enhance ET partitioning in land surface models remains unclear.

To elucidate the role of satellite vegetation parameters in estimating the ET components in land surface models, in this study we applied a representative VIC model as an example. Selecting the Loess Plateau (LP) region in China as the study area where vegetation recovery occurred. By integrating remote sensing vegetation parameters, we first investigated the influence of these parameters on the performance of ET partitions at a point scale. Our study then identified the sensitivity of the ET components to the dynamics of the LAI and fraction of vegetation coverage (FVC) under different climatic conditions. Finally, we explored the responses of ET components to vegetation greening at a regional scale in the Loess Plateau. This study enhances ET components estimation accuracy by integrating satellite vegetation parameters. Such integration provides a reference for accurately assessing water consumption

in ecological projects and studying water use efficiency in agriculture.

2. Data and methods

2.1. Study area

The LP is situated in the upper and middle reaches of the Yellow River in China and covers a total area of 632,520 km² (Fig. 1a). The region experiences a continental monsoon climate characterized by hot and rainy summers and cold and dry winters. The precipitation distribution is spatially uneven, with an annual precipitation of approximately 200 mm in the northwest and 750 mm in the southeast (Liu et al. 2023). In terms of precipitation conditions, the LP region can be divided into humid (HU), subhumid (SH), arid (AR), and semi-arid (SA) zones. The annual ET in the region is around 390 mm, increasing at a rate of 5.73 mm yr⁻¹ (Jiang et al. 2022). Around 2000, the Chinese government initiated the Grain for Green Project to restore the ecological environment in the LP (Jiang et al. 2021; Zhang et al. 2022), leading to significant vegetation greening (Fig. 1b, c). The predominant vegetation types in the area include grasslands, forests, and shrubs, with vegetation improving gradually from the northwest to the southeast (Fig. 1a). The extensive range of climatic conditions and pronounced vegetation variation renders the LP favorable for detecting the role of satellite vegetation products in partitioning ET with generalizable findings.

2.2. Data availability

The basic inputs for the VIC model include meteorological data, soil parameters, vegetation parameters, land cover types, and topographic data. Meteorological data on precipitation, maximum and minimum temperatures, and relative humidity were obtained from the China Meteorological Administration (<https://data.cma.cn/>). In this study, 571 sites in and around the LP for which these data were available were selected for spatial interpolation (Jiang et al. 2022; Meng et al. 2017; Xie et al. 2015). The temporal scale of the data is daily, from 2000 to 2020. For subsequent experiments, meteorological data were interpolated at resolutions of 0.01° and 0.0625°. The 0.01° data were used to drive the model for evaluation and point-scale experiments, whereas the 0.0625° data were employed to simulate the ET components across the entire LP. The soil and vegetation parameters were obtained from widely used datasets provided via the VIC website (<https://vic.readthedocs.io/en/master/Datasets/Datasets/>). Nijssen et al. (2001) compiled and released this dataset, which has been widely utilized. Land cover types were derived from Landsat TM images to generate a multi-year 1 km resolution raster dataset of land cover in China, available at the National Earth System Science Data Center (<https://www.geodata.cn/>). During the study period from 2000 to 2020, there was minimal change in land cover types in the study area; thus, we used data from 2010 as the basis. Topographic data were acquired using a digital elevation model provided by the United States Geological Survey (<https://earthexplorer.usgs.gov/>) and employed for accurate elevation during site validation and point experiments.

The satellite vegetation parameters within the study area were represented by the LAI and FVC, both of which were obtained from the Global Land Surface Satellite (GLASS, <https://www.geodata.cn/>) (Liang et al. 2021). The GLASS LAI product derived from MODIS surface reflectance data using a bidirectional long short-term memory model (Ma and Liang 2022; Xiao et al. 2014; Xiao et al. 2016). This model effectively utilizes global LAI datasets, along with temporal and spectral information from MODIS surface reflectance. The GLASS FVC product was developed using a multivariate adaptive regression spline approach based on MODIS data (Yang et al. 2016). The FVC product has been intensively evaluated using high-resolution satellite and ground measurement data with favorable performance (Jia et al. 2016; Jia et al. 2018).

To evaluate the ET and its components estimated using the VIC

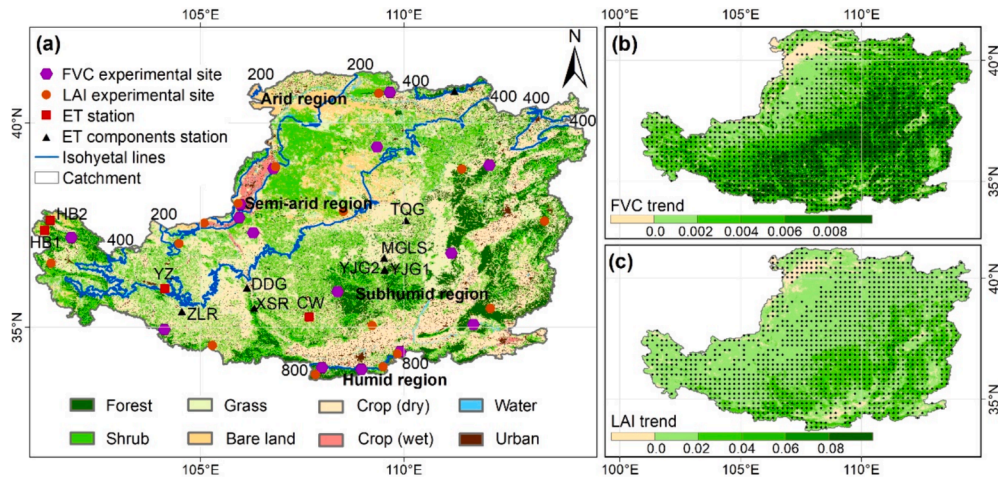


Fig. 1. (a) The locations of observation sites for ET and its components, experimental point locations, vegetation types, and precipitation zoning on the LP, trends and significant ($p < 0.05$) regions of FVC (b) and LAI (c) change in the LP from 2000 to 2020.

model, in this study we leveraged multiple covariance flux towers and field experimental sites. The observational data for ET were obtained from covariance flux towers, whereas the ET components (e.g., E_t , E_s , E_c) were derived from diverse field experiments. Detailed information and references are presented in Table 1 and 2. E_t was predominantly observed using the sap flow method, E_s using a micro-lysimeter, and E_c using a pluviometer. Additionally, owing to the challenges in acquiring experimental data on a daily scale, the evaluation of ET components was conducted on a monthly scale. Considering the spatial representativeness of the field experimental sites, we conducted model validation at a spatial resolution of 0.01° (approximately 1 km^2 for a grid cell). Pearson correlation coefficient (R), root mean square error (RMSE), and bias metrics were used to evaluate model accuracy.

2.3. Land surface model for ET partitioning

The VIC model (version 4.2. d) was used to partition ET (Liang et al. 1994). VIC is widely recognized as a land surface hydrological model with extensive applications in Earth system science and hydrology-related engineering (Jiang et al. 2022; Leng et al. 2015; Long et al. 2014). It utilizes regular grid cells to simulate surface energy and water balance. Within each grid cell, the model considers multiple sub-grid cells representing various vegetation types and bare land. The model calculates water and energy balances for each land cover type at a sub-grid scale, then aggregates these according to the proportions of each land cover type within the grid.

The VIC model is capable of estimating four ET components: E_s , E_t , E_c , and E_{sn} . The Penman–Monteith equation was first used to model the potential ET before calculating the actual E_s based on the soil moisture function. VIC then delineated ET based on internal vegetation cover calculations within each grid (Fig. 2a), which can be expressed by the following formula:

Table 1
Basic information for ET observations on Loess Plateau.

Flux station	Lat., Lon.	Year(month)	Vegetation type
Haibei shrubland (HB1)	37.62°, 101.32°	2002–2004 (1–12)	OSH
Haibei alpine Tibet (HB2)	37.37°, 101.18°	2002–2004 (1–12)	GRA
Changwu (CW)	35.25°, 107.68°	2008–2009 (7–9)	GRA
Yuzhong (YZ)	35.95°, 104.13°	2008–2009 (7–9)	GRA

$$ET = \sum_{n=1}^N C_n \bullet (E_{C_n} + E_{t_n}) + C_{N+1} \bullet E_s + E_{sn}, \quad (1)$$

where C_n represents the FVC of the n th vegetation type, C_{N+1} is the bare land fraction. Under default conditions, when the VIC model calculates the ET component within grid cells, it assumes uniform vegetation coverage (e.g., forest or shrubs) for sub-grid land cover types categorized as vegetation, that is, $FVC=1$.

The computation of ET in the VIC model was based on the constrained Penman–Monteith equation, where the aerodynamic resistance was set to zero. This simplification resulted in the Penman equation being employed to calculate potential ET:

$$E_p = \frac{\Delta(R_n - G) + \rho_a C_p D / r_a}{\lambda(\Delta + \gamma)}, \quad (2)$$

where E_p represents potential ET (mm day^{-1}), and Δ signifies the slope of the saturation vapor pressure curve at the given temperature (Pa K^{-1}), dependent on temperature. R_n is the net radiation (W m^{-2}), G is the ground heat flux (W m^{-2}), ρ_a is the density of air at constant pressure (kg m^{-3}), C_p represents the specific heat of the air ($\text{J kg}^{-1} \text{K}^{-1}$), D is the vapor pressure (kg m^{-3}), λ is the latent heat of vaporization (J kg^{-1}), γ is the psychrometric constant (Pa K^{-1}), r_a is the aerodynamic resistance (s m^{-1}), and r_a is calculated as such (Monteith et al. 1994):

$$r_a = \frac{1}{C_w u_n(Z_2)}, \quad (3)$$

where $u_n(Z_2)$ is the wind speed at the n th level of surface cover class Z_2 , and C_w is the transfer coefficient for water which is estimated based on the atmospheric stability as follows (Louis 1979):

$$C_w = 1.351 \bullet a^2 \bullet F_w, \quad (4)$$

where a^2 is the drag coefficient for the case of near-neutral stability given by:

$$a^2 = \frac{K^2}{\left[\ln \left(\frac{Z_2 - d_0}{Z_0} \right) \right]^2}, \quad (5)$$

where K is von Karman’s constant and the VIC model takes 0.4, d_0 is the zero plane displacement height, and Z_0 is the roughness length. F_w in Eq. (4) is calculated below:

Table 2

Basic information for ET components observations. The tick (✓) means the data are available. ENF is evergreen needleleaf forest, DBF is deciduous broadleaf forest, and DNF is deciduous needleleaf forest, the same below.

Station	Lat., Lon.	Et	Es	Ec	Year (month)	Method	Vegetation type	Reference
Tuqiaogou (TQG)	37.62°, 110.05°	✓	✓	✓	2003–2004 (5–10)	Micro-lysimeter, portable photosynthesis system	ENF	(Tian 2005)
Yangjuangou (YJG1)	36.70°, 109.52°			✓	2013–2014 (5–9)	Sap flow, micro-lysimeter	DBF	(Jiao et al. 2015)
Yangjuangou (YJG2)	36.40°, 109.52°	✓	✓	✓	2015–2016 (6–9)	Sap flow, micro-lysimeter	DBF	(Jiao et al. 2018)
Diediegou (DDG)	35.97°, 106.15°	✓			2006 (6–9)	Water balance, thermal dissipation probes, micro-lysimeter, pluviometer	DNF	(Liu 2008)
Xiangshui River (XSR)	35.47°, 106.33°			✓	2015 (5–10)	Pluviometer	DNF	(Liu et al. 2017)
Mt daqingshan (MDQS)	40.78°, 111.25°			✓	2016 (6–9)	Pluviometer	DBF	(Wang et al. 2017)
Zuli River (ZLR)	35.39°, 104.55°		✓		2011 (5–9)	Pluviometer	ENF	(Fang et al. 2013)

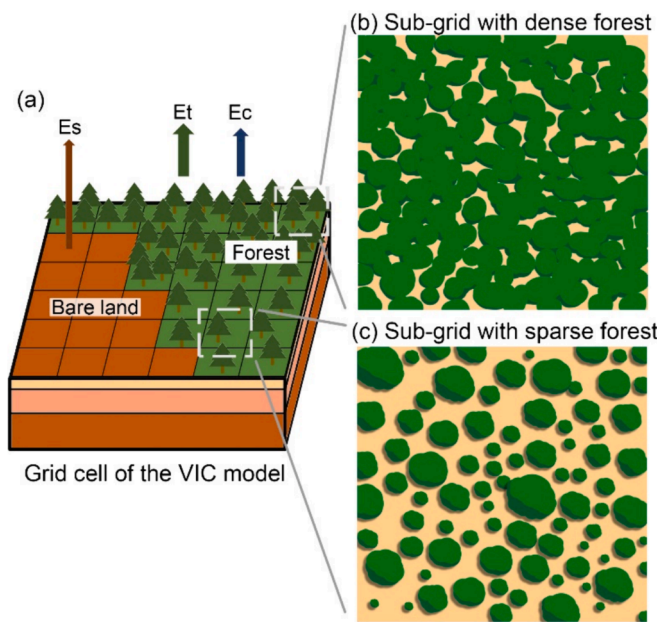


Fig. 2. (a) A brief schematic representation of ET partitioning based on vegetation cover in the VIC model, (b) sub-grid with dense forest cover, and (c) sub-grid with sparse forest cover.

$$F_w = 1 - \frac{9.4Ri_B}{1 + c \cdot |Ri_B|^{1/2}}, Ri_B < 0 \quad (6)$$

$$F_w = \frac{1}{(1 + 4.7Ri_B)^2}, 0 \leq Ri_B \leq 0.2 \quad (7)$$

where Ri_B is the bulk Richardson number, and c is expressed as (Liang et al. 1994):

$$c = 49.82 \cdot \alpha^2 \cdot \left(\frac{z_2 - d_0}{z_0} \right). \quad (8)$$

For the ET components, Ec is calculated as follows:

$$Ec = f \cdot \left(\frac{W_i}{W_{im}} \right)^{\frac{2}{3}} E_p \frac{r_a}{r_a + r_o}, \quad (9)$$

where f is the fraction of the time step at which Ec occurs, W_i is the amount of water that the canopy intercepts (mm), and W_{im} is the maximum amount of water that the canopy can intercept (mm). W_{im} can be calculated based on the LAI as follows: $W_{im} = K_L \cdot LAI$, where K_L is a

constant, taken to be 0.2 mm following (Dickinson 1984). Finally, r_o represents the architectural resistance caused by the humidity gradient between the vegetation canopy leaves and the air above them (s/m).

Et is calculated as follows:

$$Et = (1 - f)E_p \frac{r_a}{r_a + r_o + r_c} + f \cdot \left(1 - \left(\frac{W_i}{W_{im}} \right)^{\frac{2}{3}} \right) E_p \frac{r_a}{r_a + r_o + r_c}, \quad (10)$$

where r_c is the canopy resistance (s/m) given by:

$$r_c = \frac{r_{oc}g_{sm}}{LAI}, \quad (11)$$

where r_{oc} is the minimum canopy resistance and g_{sm} is the soil moisture stress factor depending on the water availability in the root zone. The expression of g_{sm} is as follows:

$$g_{sm}^{-1} = \begin{cases} 1, & W_j \geq W_j^{cr} \\ \frac{W_j - W_j^w}{W_j^{cr} - W_j^w}, & W_j^w \leq W_j < W_j^{cr} \\ 0, & W_j < W_j^w \end{cases}, \quad (12)$$

where W_j is the soil moisture content in layer j , $j = 1, 2$, and 3 . W_j^{cr} is the critical value above which transpiration is not affected by moisture stress in the soil, and W_j^w is the soil moisture content at the permanent wilting point.

Es is only computed for bare land, and was assumed from Layer 1. When this layer reaches saturation, Es is computed at the potential evaporation rate; otherwise, its evaporation vary based on differences in the infiltration capacity, topography, and soil characteristics. The equation for calculating Es is as follows:

$$Es = E_p \left(\int_0^{A_s} dA + \int_{A_s}^1 \frac{i_0}{i_m (1 - (1 - A)^{1/b_i})} dA \right), \quad (13)$$

where i_m is the maximum infiltration capacity (mm), A_s is the fraction of saturated bare soil, and i_0 is the corresponding point-infiltration capacity. A is the fraction of the area for which the infiltration capacity is less than the current infiltration capacity i , and b_i is the infiltration shape parameter.

Esn is directly calculated based on the adjusted energy balance. Energy exchange between the atmosphere, canopy layer, and snow occurs only at the surface layer. For specific details on the calculation of Esn as well as the mentioned parameters and variables, please refer to the original VIC paper (Liang et al. 1994). For model calibration and validation, the parameter values, except for LAI and FVC, were obtained from Jiang et al. (2022), in which the water balance, including the total

ET and water discharge, was well evaluated, and acceptable performance was achieved.

2.4. Dynamic vegetation parameters in ET partitioning

The VIC model considers both the water constraints within the grid cells and the energy balance process, endowing it with the advantage of reflecting clear physical processes and reliable performance. Previous studies predominantly used the VIC model's default/static assumption, where LAI was prescribed with 12-month climatological values, and FVC was defined as the proportion of vegetated sub-grid cells within each grid cell. Under this assumption, VIC only considers the seasonal variation of LAI and a fixed FVC (i.e., FVC=1). Thus it disregards inter-annual variations in LAI and both inter- and intra-annual variations in FVC. According to the computation of W_{im} in Eq. (9) and r_c in Eq. (10), variations in LAI strongly influence the estimation of E_c and E_t . As illustrated in Eq. (1), the FVC within a grid cell is also important in ET partitioning. While a fixed FVC may introduce minor errors in densely vegetated areas (Fig. 2b), substantial uncertainties will arise in sparsely vegetated regions (Fig. 2c). Therefore, the static assumption of vegetation conditions introduces considerable uncertainty into ET estimation in the VIC model.

In this study, we examine a dynamic vegetation framework within VIC to address the limitations of the default assumption. In this framework, daily-scale dynamic LAI and FVC data are integrated into the forcing dataset, replacing the default/static vegetation information. When employing dynamic vegetation parameters to partition ET, the GLASS LAI are used to compute E_c and E_t for the computation of W_{im} in Eq. (9) and r_c in Eq. (10), and the GLASS FVC are used to partition ET components according to Eq. (1). We prepared a daily scale satellite vegetation parameter-driven model to explore the effect of dynamic vegetation parameters on ET partitioning.

We designed two simulation scenarios at point scales: one using the default vegetation conditions (static LAI and FVC), and the other incorporating satellite vegetation parameters (dynamic LAI and FVC). We calculated the differences in the ET components between the two scenarios at three temporal scales: annual averages, inter- and intra-annual variations. The configuration of the experimental sites is elaborated in detail in Section 2.5.

To investigate the sensitivity of ET and its components to dynamic vegetation conditions, we further designed a series of scenarios with various scale factors for the LAI and FVC at point scales. Based on the mean LAI in the study area (LAIs = 1.23 m² m⁻²), we prescribed scale factors varying from zero to 1.5; thus, 15 scenarios were evaluated with mean LAI values ranging from zero to 1.85 m² m⁻². Given the mean FVC in the study area (FVC=0.4), the scale factors were prescribed from 0.1 to 1.1, resulting in 11 scenarios with FVC values ranging from 0.04 to 0.41. It should be noted that the default FVC in the VIC was 1.0, as explained in Subsection 2.3. The upper limit of the FVC was 1.0; therefore, we considered the maximum scale factor value only up to 1.1 times the original FVC to prevent regions with high FVC from exceeding this limit.

To explore the effect of temporal variations in LAI and FVC on the VIC model simulation of ET and its components, we proposed the following sensitivity coefficient (Sankarasubramanian et al. 2001):

$$S_x = \frac{dE/E}{dx/x} = \frac{dE}{dx} \cdot \frac{x}{E}, \quad (14)$$

where E represents the ET and its components, x represents the dynamic vegetation parameters, and S_x is the sensitivity coefficient. S_x can be understood as the percentage change in the ET and its components resulting from a certain percentage change in the dynamic vegetation parameters over time. A larger absolute value of the sensitivity coefficient indicates a stronger effect of the factor on the ET and its components.

2.5. Experimental design

The effects of dynamic vegetation on ET partitioning may vary with climatic conditions. We examined this effect at a point scale and selected study sites from four different climatic conditions according to long-term average annual precipitation: AR (annual precipitation < 200 mm), SA (annual precipitation between 200 and 400 mm), SH (annual precipitation between 400 and 800 mm), and HU (annual precipitation > 800 mm) regions. The experimental sites were selected according to three criteria: (1) vegetation parameters (LAI or FVC) at the study site varied significantly ($P < 0.05$) among years during the study period, assessed with the Mann-Kendall trend test; (2) vegetation type at the sites primarily specified as forest; and (3) relatively uniform spatial distribution of the vegetation across the entire study area, with each site covering at least six grid cells (approximately 6 km²) to eliminate potential uncertainties from variability in individual grid cells. Based on these criteria, we defined 15 sites for the four climatic conditions, as shown in Table 3. The distribution of the 15 sites is shown in Fig. 1a along with the vegetation types and stratum boundaries.

3. Results

3.1. Model evaluation

First, we evaluated the VIC model with and without dynamic satellite vegetation parameters. As shown in Fig. 3, the VIC model was capable of simulating the temporal variations in ET. Under default conditions, the average R value was 0.46, with a lower accuracy observed at specific stations (Fig. 3c). Following the incorporation of the satellite vegetation parameters, the VIC model demonstrated improved ET simulation accuracy, with an average R value of 0.75 and an average RMSE of 1.25 mm day⁻¹.

For ET partitioning, the VIC model with default vegetation tended to overestimate E_t and E_c (Figs. 4 and 5) and significantly underestimate E_s (Fig. 6). Upon the inclusion of satellite vegetation parameters, the model demonstrated marked improvements: a substantial increase in R for E_t by 0.89 (1620 %), with a mean decrease in RMSE of 12.68 mm mon⁻¹ (65.77 %), and an average reduction in bias of 124.83 % (86.52 %). Similarly, it raised the average R for E_c by 0.48 (141.18 %), leading to an average decrease in RMSE by 17.50 mm mon⁻¹ (80.52 %) and an average reduction in bias by 676.28 % (94.87 %). In the simulation of E_s , the inclusion of satellite vegetation parameters yielded an average R of 0.73, an average RMSE of 5.03 mm mon⁻¹, and an average bias of 40.02 %.

3.2. Influence of dynamic LAI on ET partitioning

We first evaluated the influence of dynamic LAI on ET partitioning under the four climatic conditions. After incorporating dynamic LAI into the VIC model (Fig. 7), the overall mean of ET decreased slightly, with an average reduction of 6.98 mm yr⁻¹ (2.25 %). Among the different ET components, dynamic LAI resulted in increased E_s and E_t and decreased E_c and E_{sn} , except under AR conditions. Under different climatic conditions, the differences induced by dynamic LAI gradually diminished with increasing precipitation. In HU regions (Fig. 7d), the disparities in the ET components narrowed to within 2 %.

Incorporation of dynamic LAI markedly reshaped the components of

Table 3
Climatic conditions and study sites Settings.

Annual precipitation	Climatic conditions name	Number of experimental sites
0–200 mm	Arid region (AR)	3
200–400 mm	Semi-arid region (SA)	3
400–800 mm	Subhumid region (SH)	6
800–1200 mm	Humid region (HU)	3

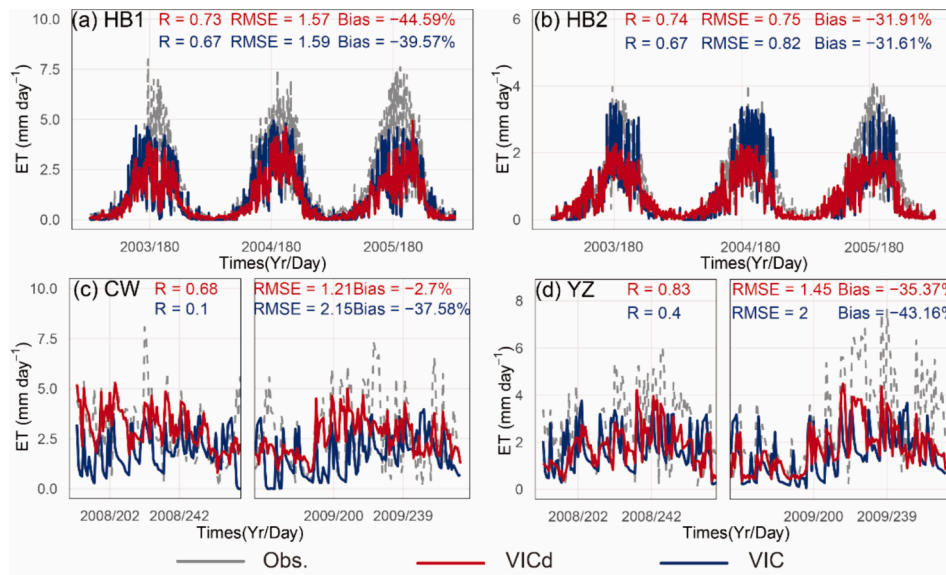


Fig. 3. The comparison of observed ET from four covariance flux towers (Obs.) with ET simulated by the VIC model under default conditions (VIC) and with the integration of dynamic vegetation parameters (VICd) on a daily scale at: (a) HB1 Station, (b) HB2 Station, (c) CW Station, (d) YZ Station.

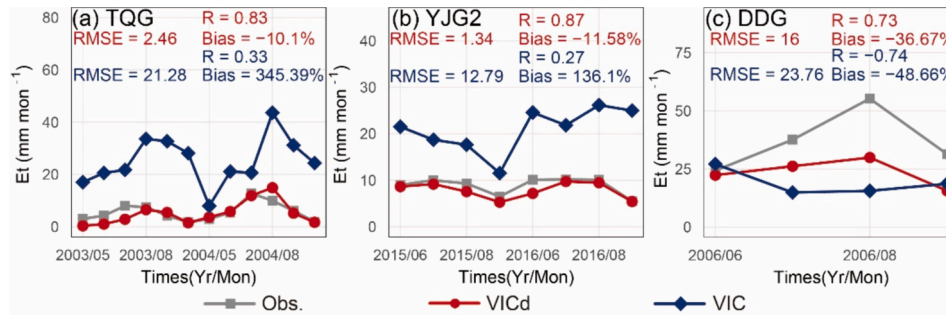


Fig. 4. The comparison of observed Et from three field experiment stations (Obs.) with Et simulated by the VIC model under default conditions (VIC) and with the integration of dynamic vegetation parameters (VICd) on a monthly scale at: (a) TQG Station, (b) YJG2 Station, (c) DDG Station.

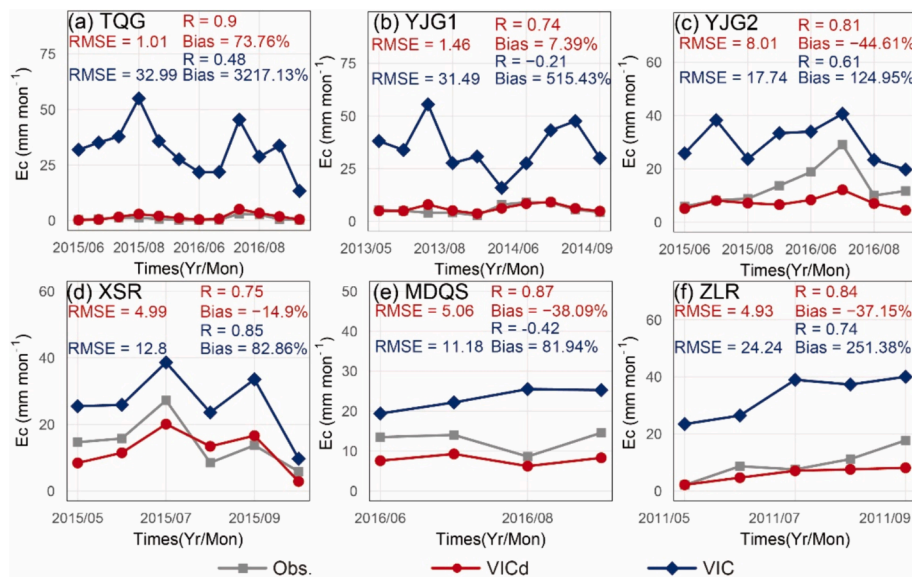


Fig. 5. The comparison of observed Ec from six field experiment stations (Obs.) with Ec simulated by the VIC model under default conditions (VIC) and with the integration of dynamic vegetation parameters (VICd) on a monthly scale at: (a) TQG Station, (b) YJG1 Station, (c) YJG2 Station, (d) XSR Station, (e) MDQS Station, (f) ZLR Station.

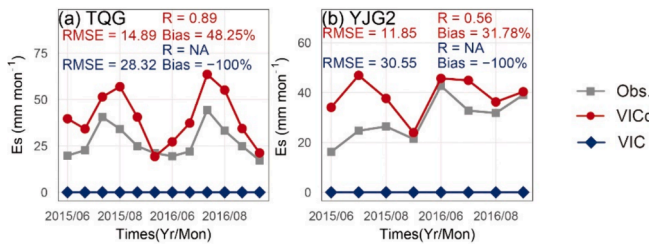


Fig. 6. The comparison of observed Es from two field experiment stations (Obs.) with Es simulated by the VIC model under default conditions (VIC) and with the integration of dynamic vegetation parameters (VICd) on a monthly scale at: (a) TQG Station, (b) YJG2 Station.

ET regarding interannual variations (Fig. 8), primarily resulting in an increase in Es and Et and a decrease in Ec and Esn. Notably, the inter-annual trends of Ec and Et were also altered, with accelerated interannual variation in Et in AR and SA regions albeit delayed change in Ec (Fig. 8a, b). Conversely, the Ec trend was accelerated in the SH and HU regions (Fig. 8c, d). In comparison, dynamic LAI incorporation predominantly affected the Et and Ec components related to intra-annual variations (Fig. 9). In particular, the peak value of Et occurred earlier throughout the year (Fig. 9b, c, d), resulting in a deceleration of the intra-annual variation in Ec (Fig. 9a, b).

ET increased with higher LAI coefficients, exhibiting a pattern of rapid growth followed by a slower increase (Fig. 10). In particular, the proportion of Es decreased as LAI increased, showing a pattern of rapid decline followed by a gradual decrease. Alternatively, the proportion of Et initially increased and then decreased; this pattern became more pronounced with increasing precipitation in the respective regions. In turn, the proportion of Ec increased linearly, whereas that of Esn did not markedly change.

Moreover, the influence of the LAI on ET and its components gradually diminished from AR to HU regions (Table 4). Among the ET components, Et and Ec exhibited the highest sensitivity to LAI changes, whereas the sensitivities of Es and Esn were relatively low.

3.3. Influence of dynamic FVC on ET partitioning

After incorporating dynamic FVC into the VIC model (Fig. 11), the overall mean of ET slightly increased, with an average rise of 17.15 mm yr⁻¹ (5.35%). Among the different ET components, Et, Ec, and Esn were decreased, with Et experiencing the most notable decline, whereas Es was improved. Similar to the results obtained for dynamic LAI, the differences induced by dynamic FVC gradually diminished with increased humidity. Notably, in the absence of dynamic FVC, over 70% of the Es was allocated to other ET components in AR and SA regions (Fig. 11a, b), introducing substantial biases in the simulation of other ET components.

The effect of dynamic FVC was relatively small for interannual variations; however, it enhanced the ET growth rate in the AR region

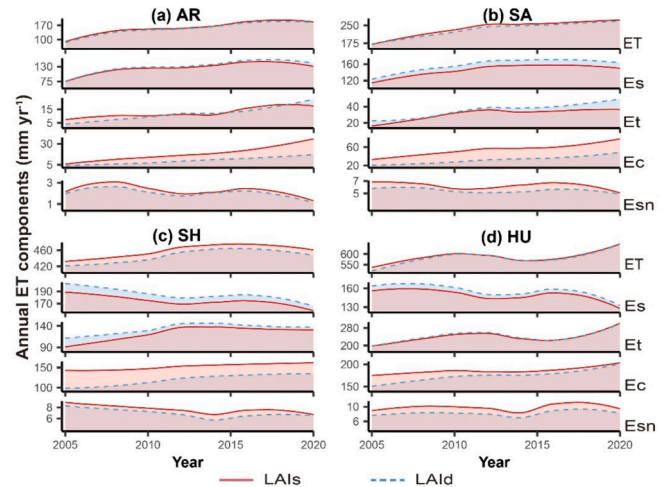


Fig. 8. Inter-annual variations in simulated ET and its components under different LAI conditions across four climatic conditions: (a) AR, (b) SA, (c) SH, and (d) HU. LAId represents dynamic LAI, while LAIs represents static/default LAI.

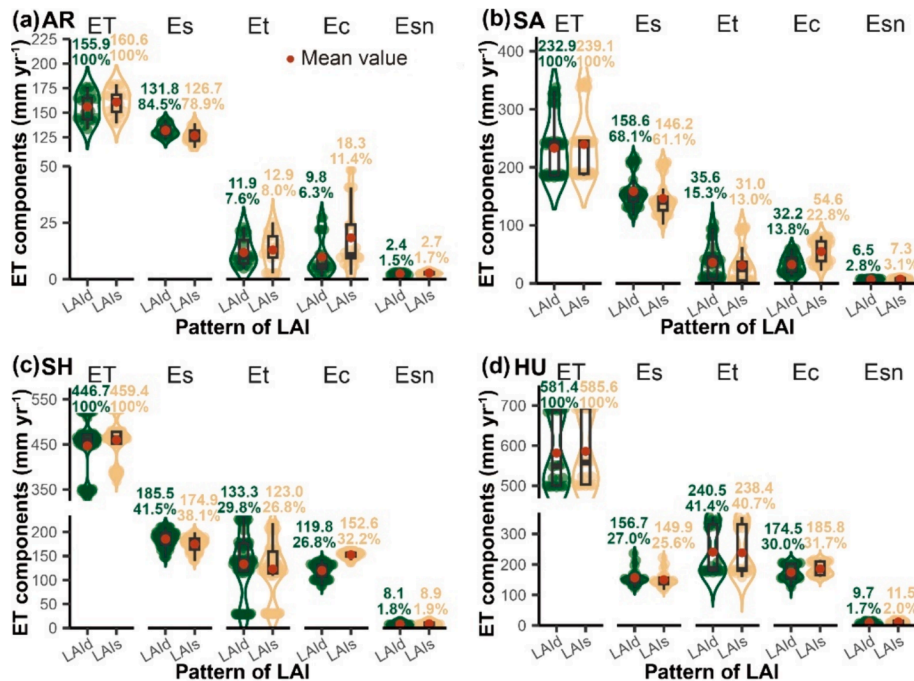


Fig. 7. Simulated ET and its components under different LAI conditions across four climatic conditions: (a) AR, (b) SA, (c) SH, and (d) HU. LAId represents dynamic LAI, and LAIs represents static/default LAI.

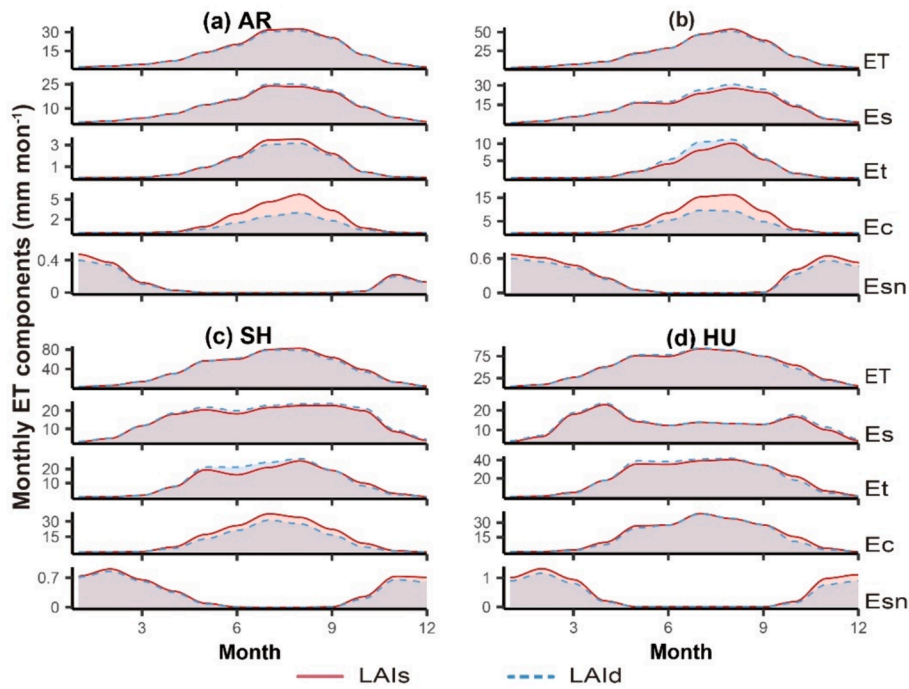


Fig. 9. Intra-annual variations in simulated ET and its components under different LAI conditions across four climatic conditions: (a) AR, (b) SA, (c) SH, and (d) HU. LAI_d represents dynamic LAI, while LAI_s represents static/default LAI.

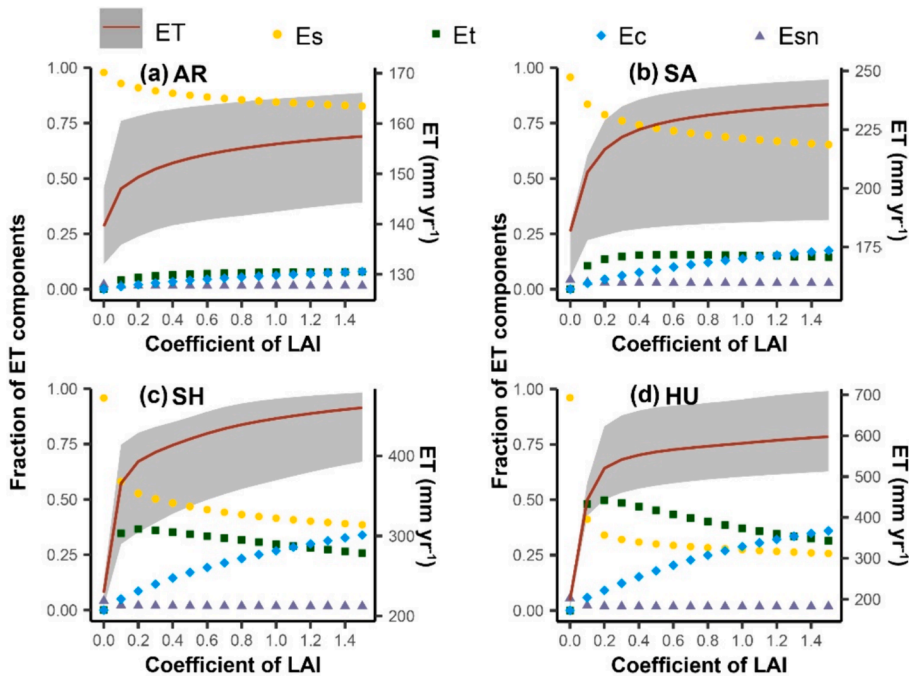


Fig. 10. Sensitivity of ET and the components to LAI in VIC modeling across four climatic conditions: (a) AR, (b) SA, (c) SH, (d) HU. The shaded area represents the interquartile range of the ET, with the lower boundary corresponding to the 25% and the upper boundary to the 75%. The coefficient of LAI indicates the change magnitude of LAI relative the normal condition.

(Fig. 12). Alternatively, dynamic FVC had minimal influence on the overall magnitude and trend of ET with regard to intra-annual variations, although it delayed the peak value of ET throughout the year. The effects of dynamic FVC on ET components were mainly manifested in Es and Et, with Es exhibiting a transition from negligible to notable intra-annual dynamics, and Et showing a substantial reduction (Fig. 13). Increasing humidity also gradually diminished the influence of dynamic

FVC on these components.

ET gradually increased with increasing FVC coefficients in the AR and SA regions (Fig. 14a, b), whereas in the SH and HU regions, it initially increased and then decreased with increasing FVC coefficients (Fig. 14c, d). In particular, the proportion of Es decreased linearly with increasing FVC, that of Et showed a fluctuating upward pattern, whereas that of Ec exhibited logarithmic growth.

Table 4
The sensitivity of ET and its components to changes in LAI.

Climate zone	ET	Et	Ec	Es	Esn
AR	1.16 ± 0.88	3.00 ± 2.20	2.40 ± 1.84	0.98 ± 0.75	-1.17 ± 0.93
SA	0.44 ± 0.21	0.93 ± 0.57	1.05 ± 0.56	0.27 ± 0.12	-0.42 ± 0.28
SH	0.11 ± 0.56	0.08 ± 1.38	1.27 ± 0.58	-0.53 ± 0.23	-1.24 ± 0.87
HU	0.20 ± 0.22	0.43 ± 0.62	0.81 ± 0.37	-0.62 ± 0.55	-0.44 ± 0.31

Moreover, the influence of FVC on ET and its components gradually decreased from the AR to HU regions (Table 5). Among the ET components, Et exhibited the highest sensitivity to changes in FVC, followed by Ec, Es, and Esn. Notably, ET and its components were more sensitive to changes in FVC than to changes in LAI.

3.4. Spatial variation of ET components on the LP

Given the favorable performance of VIC incorporating dynamic vegetation, we simulated the ET and its components on the LP using the VIC model under two scenarios: with the inclusion of satellite vegetation parameters or in a static or default state. Subsequently, the spatial differences between the two scenarios were compared (Fig. 15). Across both scenarios, ET and its components exhibited an increasing trend from the northwest to southeast of the LP. Notably, with the incorporation of the satellite parameters, we observed a substantial increase in Es across the LP, particularly in the central forested regions (Fig. 15d, e, f). However, the inclusion of satellite dynamic vegetation parameters led to an overall decrease in both Et and Ec in the LP. Specifically, Et exhibited substantial reductions in the central and eastern regions (Fig. 15i), whereas Ec showed prominent decreases in the central region (Fig. 15l), with reductions of 139.63 and 41.88 mm yr⁻¹, respectively.

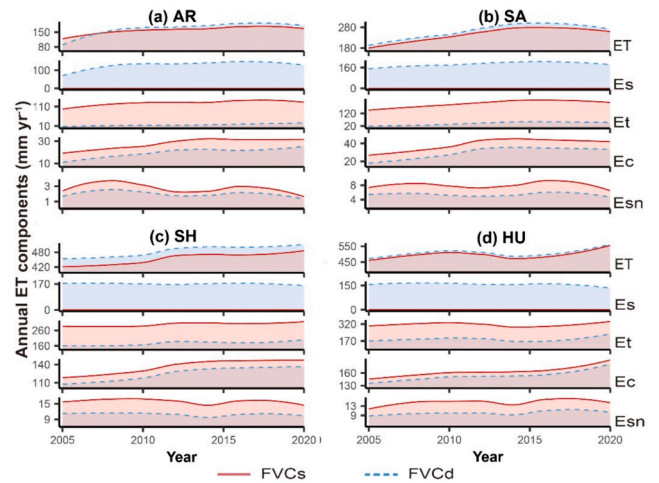


Fig. 12. Inter-annual variations in simulated ET and its components under different FVC conditions across four climatic conditions: (a) AR, (b) SA, (c) SH, and (d) HU. LAId represents dynamic FVC, while LAIs represents static/default FVC.

4. Discussion

4.1. Mechanism of ET partitioning in land surface hydrological modeling

The inclusion of dynamic LAI had a more pronounced influence than the static LAI on the interannual variability of Ec and ET as determined through VIC modeling. The dynamic LAI increased the interannual variability of Et (Fig. 8) relative to that using the VIC model with its default LAI (Liang et al., 1994). Under this default or static application, the LAI exhibited only intra-annual variability without interannual changes, resulting in a smoother Et variation profile (Fig. 16a). The inclusion of the dynamic LAI allowed the model to capture the interannual variability in vegetation growth. An increase in LAI directly augments the leaf stomatal conductance, leading to a reduction in transpiration

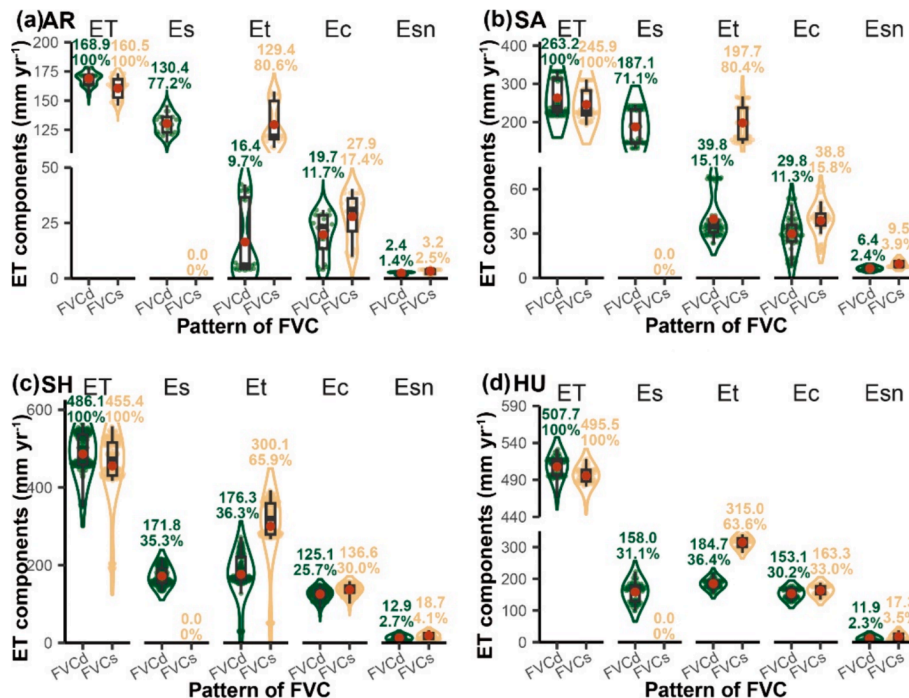


Fig. 11. Simulated ET and its components under different FVC conditions across four climatic conditions: (a) AR, (b) SA, (c) SH, and (d) HU. FVCd represents dynamic FVC, and FVCs represents static/default FVC.

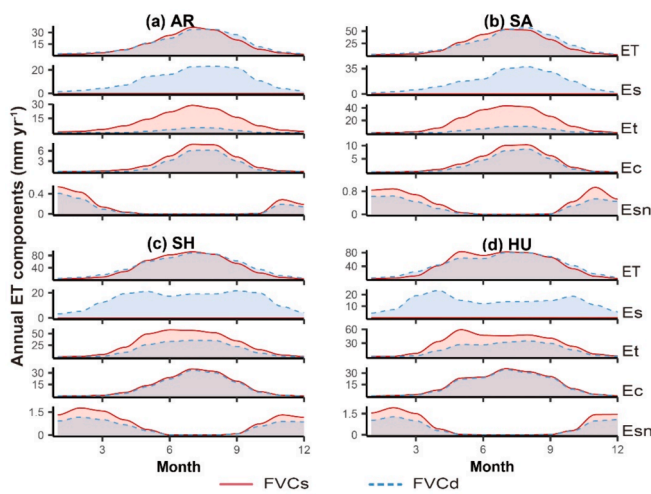


Fig. 13. Intra-annual variations in simulated ET and its components under different LAI conditions across four climatic conditions: (a) AR, (b) SA, (c) SH, and (d) HU. FVCd represents dynamic FVC, while FVCs represents static/default FVC.

resistance and an increase in transpiration (Meinzer and Evolution, 1993). This change was more evident in regions with limited water availability (i.e., AR and SA regions) (Fig. 8a, b). However, the VIC is sophisticated when considering soil moisture constraints on Et (Liang et al., 1994). Excessive transpiration induces soil moisture stress,

thereby restricting the increase in Et (Fig. 16b). This explains the observed trend of an initial increase, followed by a decrease in the response of Et to the LAI coefficient (Fig. 10). In turn, the increase in the LAI directly enhanced the maximum interception capacity of vegetation, resulting in a linear increase in the proportion of Ec with the increase in the LAI coefficient (Fig. 10).

The most notable effect of dynamic FVC inclusion in the model was observed with regard to altering the pattern of ET partitioning, allowing for the simulation of forest gaps (Fig. 16b). This stems from the default setting of the VIC model, wherein during the computation of the vegetated tile, it is assumed that the tile is entirely veiled by vegetation (i.e., FVC=1.0) (Liang et al., 1994). Consequently, the model failed to account for the Es within these designated subgrids (Fig. 16a). With the incorporation of dynamic FVC, the model divides the grid cells based on the actual FVC at the current time for each subgrid, enabling the simulation of Es from forest gaps (Fig. 16b). Under water-limited conditions, that is, in AR and SA regions, the presence of forest gaps becomes more apparent. This explains why the ratio of Es to ET increased by over 70 % in AR and SA regions after introducing dynamic FVC (Fig. 11a, b). Our findings indicate that, under conditions of static vegetation cover, interstitial Es is misallocated to Et during ET partitioning, leading to an overestimation of Et. This overestimation was evident in our model validation using the field experiment results. For example, at the TQG and YJG2 sites (sites encompassing all ET components) (Fig. 4a, b; Fig. 5a, c), the VIC model under default conditions consistently overestimated both Et and Ec. Such discrepancies can engender considerable uncertainty in eco-hydrological vegetation research.

After incorporating dynamic LAI and FVC, Es increases while Et and

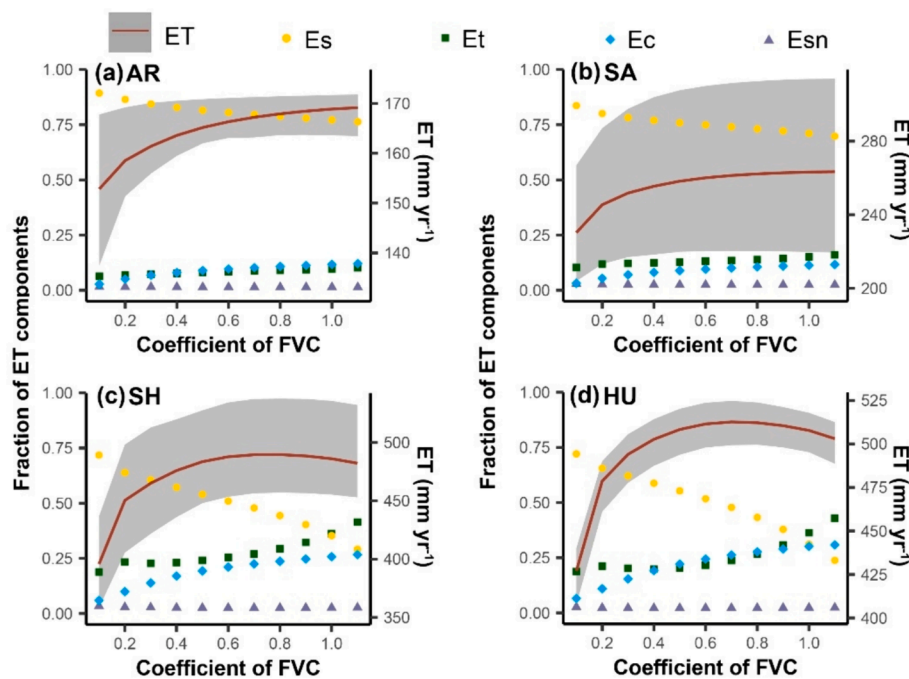


Fig. 14. Sensitivity of ET and the components to FVC in VIC modeling across four climatic conditions: (a) AR, (b) SA, (c) SH, (d) HU. The shaded area represents the interquartile range of the ET, with the lower boundary corresponding to the 25% and the upper boundary to the 75%. The coefficient of LAI indicates the change magnitude of FVC relative the normal condition.

Table 5

The sensitivity of ET and its components to changes in FVC.

Climate zone	ET	Et	Ec	Es	ESn
AR	0.98 ± 0.70	3.70 ± 3.02	1.29 ± 0.79	0.85 ± 0.63	-0.90 ± 0.76
SA	0.71 ± 0.21	1.36 ± 0.35	1.12 ± 0.63	0.42 ± 0.19	-0.43 ± 0.25
SH	0.26 ± 0.51	0.35 ± 1.07	1.03 ± 0.54	-0.15 ± 0.17	-0.72 ± 1.49
HU	0.24 ± 0.20	-0.03 ± 0.57	0.94 ± 0.44	-0.51 ± 0.03	0.86 ± 0.50

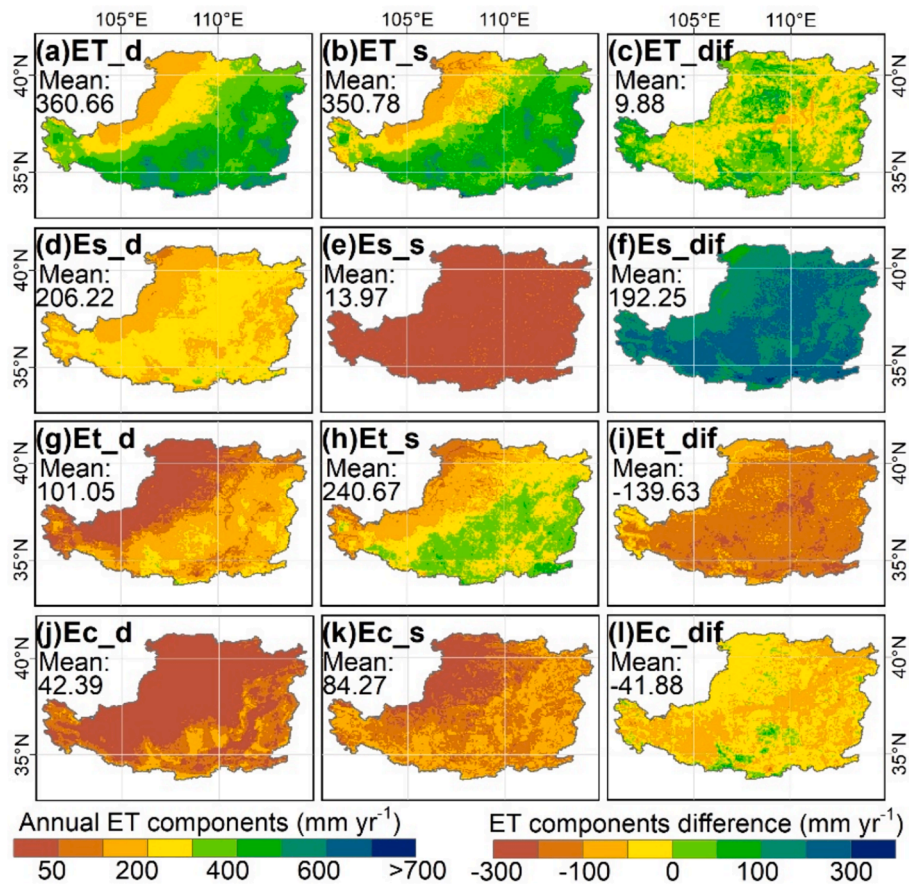


Fig. 15. ET and its components simulated by the VIC model under dynamic vegetation parameters (Column 1) and static/default conditions (Column 2), along with the differences between the two (Column 3, calculated as the dynamic vegetation parameter results minus static/default state results). Additionally, E_{sn} is not presented and discussed here due to its relatively small magnitude.

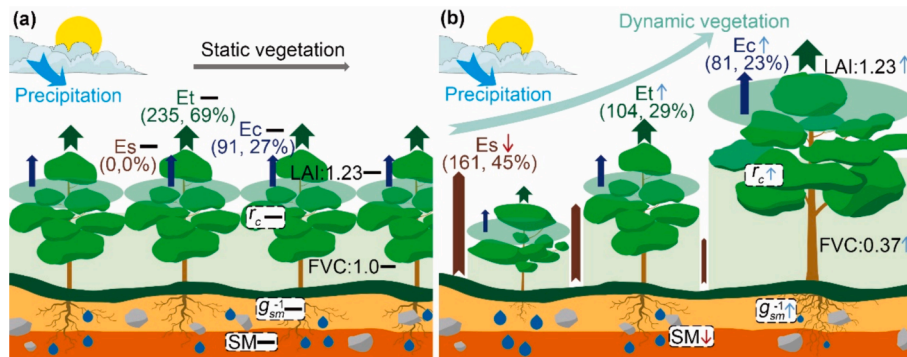


Fig. 16. Difference in VIC model-simulated ET components between static vegetation (a) and dynamic vegetation (b). Here SM represents soil moisture, g_{sm} represents the soil moisture stress factor, and r_c represents canopy resistance.

Ec decrease across the entire LP, with the greatest changes observed in the central forested regions. This adjustment reveals gaps in previous Es simulations erroneously allocated to Et and Ec. Spatially, regions with sparse vegetation in the northwest show smaller changes compared to densely forested areas in the central region, highlighting the critical need to integrate dynamic vegetation parameters for ET partitioning in forested regions.

4.2. Importance of considering vegetation dynamics for estimating ET components

Dynamic vegetation parameters in land surface modeling are

effective in reducing the uncertainty in ET partitions. Among the currently available ET component products, significant variations exist in the proportions of different components across various datasets (Talsma et al., 2018a, Talsma et al., 2018b, Bowen et al., 2019, Miralles et al. 2016, Lian et al. 2018). For example, across different datasets, the T/ET ratio ranged from < 45 % to > 80 % (Bowen et al. 2019). This variability stems from the diverse assumptions made during the allocation of ET components in different datasets, with particular uncertainty in Es estimation (Talsma et al. 2018a). Moreover, Et is generally overestimated in existing products (Good et al. 2015). Our findings indicate that incorporating dynamic vegetation parameters considerably enhances the accuracy of ET partitioning in the VIC model compared to

static vegetation conditions. This approach reduces uncertainty in Es (Fig. 6) and mitigates overestimations of Et and Ec (Figs. 4 and 5). Therefore, considering dynamic vegetation is crucial for reducing uncertainty in ET allocation.

A few studies have shown that incorporating dynamic vegetation parameters enhances the reliability of ET simulations (Cao et al. 2022; Jiang et al. 2022; Paschalis et al. 2018; Wang et al. 2014; Wei et al. 2017; Yang et al. 2023). However, these studies generally focused on a single vegetation parameter. For example, Yang et al. (2022) considered FVC but overlooked LAI, while Bai et al. (2018) concentrated solely on dynamic changes in LAI and disregard changes in FVC. Our study illustrates that FVC and LAI exert distinct yet equally significant impacts on the simulation of ET components. Specifically, FVC changes the allocation pattern of ET components in forested areas, while LAI affects intra- and inter-annual trends in ET components. Therefore, accurately simulating ET components in land surface hydrological models requires comprehensive consideration of dynamic FVC and LAI.

Vegetation dynamics from satellite retrieval offer advantages relative to vegetation growth modules in land surface models (Shu et al. 2022, Anav et al. 2013, Cadule et al. 2010). In land surface models, such as the CLM and Noah-MP, the vegetation growth module, based on vegetation physiology, incorporates the relationships between environmental variables and vegetation growth to simulate vegetation dynamics (Hosseini et al. 2022, Lawrence et al. 2019, Jasechko et al. 2013, Sato et al. 2014). However, owing to the assumptions in biophysical formulations, uncertainties in model parameters, and input data, the accuracy of these models remains problematic (Shu et al. 2022). Numerous studies have relied on satellite vegetation data to validate the performance of vegetation dynamics simulated by land surface models (Dickinson et al. 1998, Shu et al. 2022), supporting satellite vegetation data as the most dependable option for assessing genuine vegetation conditions in a given region. The vegetation dynamics module is particularly applicable for evaluating vegetation predictions and carbon cycling (Dickinson et al. 1998, Sato et al. 2014).

In the land surface models, when partitioning ET, the sensitivity to FVC was higher than that to LAI. This is because FVC directly influences the partitioning of ET component proportions. Specifically, Et showed the highest sensitivity to FVC (Table 5), primarily because in land surface models, Et is calculated only in areas with vegetation cover. Alternatively, Es in vegetated areas was suppressed. Therefore, accurately considering the dynamic changes in FVC is crucial for accurately simulating Et and Es. The FVC and LAI also have significant effects on Ec, as FVC and LAI respectively determine the spatial extent and overall magnitude of the Ec calculations. Notably, ET components exhibit heightened sensitivity to vegetation changes in AR and SA regions, where vegetation conditions are poorer, resulting in more pronounced disturbances to ET components. In particular, we focused solely on the LP region, which encompasses multiple climatic zones; however, the vegetation status within individual climatic zones may exhibit relatively uniform characteristics. Hence, we experimented with multiple vegetation parameter magnitudes to account for this variability. Similarly, to obtain the aforementioned findings, we incorporated the closely related variables LAI and FVC separately into the model and analyzed their distinct mechanisms for partitioning ET components.

5. Conclusion

This study investigated the role of satellite vegetation products in allocating ET components (i.e., Es, Et, Ec, and E_{sn}) within land surface models. We employed the VIC model, which integrates water and energy balances but lacks a dynamic vegetation module. The results indicate that although the inclusion of dynamic vegetation parameters marginally improves the ET estimation, it enhances the correlation coefficient R of the ET components by 0.70 and reduces the RMSE by 11.74 mm mon⁻¹. Among the various dynamic vegetation parameters, the inclusion of dynamic LAI alters the inter- and intra-annual variations in Et

and Ec, whereas dynamic FVC reshapes the distribution pattern of ET components, enabling the model to simulate canopy gaps in Es, thereby mitigating ET overestimation. Among different climatic zones, the effect of dynamic vegetation parameters is particularly pronounced in arid and semi-arid regions because of sparser vegetation compared with that in subhumid and humid regions. Increased vegetation led to a linear decrease in Es, a rapid initial increase in ET, followed by a gradual decrease and a linear increase in Ec, highlighting the sensitivity of ET components to vegetation dynamics. Temporally, Et exhibited the highest sensitivity to vegetation dynamics, followed by Ec and Es. Across the entire LP region, the incorporation of satellite vegetation parameters resulted in a 192.25 mm yr⁻¹ increase in Es, which was primarily concentrated in the central forested areas, whereas Et decreased by 139.63 mm yr⁻¹ and Ec decreased by 41.88 mm yr⁻¹.

Our findings underscore the notable effect of satellite vegetation parameters on the allocation of ET within land surface models, particularly highlighting how dynamic FVC alters the distribution patterns of ET components. These results provide a theoretical groundwork for more precisely evaluating the hydrological effects of ecological restoration projects and the influence of vegetation greening on the water cycle.

CRediT authorship contribution statement

Dawei Peng: Writing – review & editing, Writing – original draft, Visualization, Validation, Software, Methodology, Investigation, Funding acquisition, Formal analysis, Data curation, Conceptualization. **Xianhong Xie:** Writing – review & editing, Supervision, Project administration, Funding acquisition, Conceptualization. **Shunlin Liang:** Supervision, Conceptualization. **Yibing Wang:** Formal analysis, Conceptualization. **Arken Tursun:** Resources, Conceptualization. **Yao Liu:** Formal analysis, Conceptualization. **Kun Jia:** Conceptualization. **Han Ma:** Data curation. **Yuchao Chen:** Conceptualization.

Declaration of competing interest

The authors declare the following financial interests/personal relationships which may be considered as potential competing interests: Xianhong Xie reports financial support was provided by National Natural Science Foundation of China. Dawei Peng reports financial support was provided by State Key Laboratory of Remote Sensing Science and Beijing Engineering Research Center for Global Land Remote Sensing Products. If there are other authors, they declare that they have no known competing financial interests or personal relationships that could have appeared to influence the work reported in this paper.

Data availability

Data will be made available on request.

Acknowledgment

This study was supported by a grant from the National Natural Science Foundation of China (No. 42271021) and the Open Fund of State Key Laboratory of Remote Sensing Science and Beijing Engineering Research Center for Global Land Remote Sensing Products (Grant No. OF202407).

References

- Anav, A., Murray-Tortarolo, G., Friedlingstein, P., Sitch, S., Piao, S., Zhu, Z., 2013. Evaluation of land surface models in reproducing satellite derived leaf area index over the high-latitude northern hemisphere. Part II: earth system models. *Remote Sens.* 5, 3637–3661. <https://doi.org/10.3390/rs5083637>.
- Bai, P., Liu, X., Zhang, Y., Liu, C., 2018. Incorporating vegetation dynamics noticeably improved performance of hydrological model under vegetation greening. *Sci. Total Environ.* 643, 610–622. <https://doi.org/10.1016/j.scitotenv.2018.06.233>.

- Bastiaanssen, W.G.M., Menenti, M., Feddes, R.A., Holtslag, A.A.M., 1998a. A remote sensing surface energy balance algorithm for land (SEBAL). 1. Formulation. *J. Hydrol* 212–213, 198–212. [https://doi.org/10.1016/S0022-1694\(98\)00253-4](https://doi.org/10.1016/S0022-1694(98)00253-4).
- Bastiaanssen, W.G.M., Pelgrum, H., Wang, J., Ma, Y., Moreno, J.F., Roerink, G.J., van der Wal, T., 1998b. A remote sensing surface energy balance algorithm for land (SEBAL): Part 2: Validation. *J. Hydrol* 212–213, 213–229. [https://doi.org/10.1016/S0022-1694\(98\)00254-6](https://doi.org/10.1016/S0022-1694(98)00254-6).
- Bohn, T.J., Vivoni, E.R., 2016. Process-based characterization of evapotranspiration sources over the North American monsoon region. *Water Resour. Res.* 52, 358–384. <https://doi.org/10.1002/2015wr017934>.
- Bowen, G.J., Cai, Z., Fiorella, R.P., Putman, A.L., 2019. Isotopes in the Water Cycle: Regional- to Global-Scale Patterns and Applications. *Annu. Rev. Earth Pl. Sc.* 47, 453–479. <https://doi.org/10.1146/annurev-earth-053018-060220>.
- Cadule, P., Friedlingstein, P., Bopp, L., Sitch, S., Jones, C.D., Ciais, P., Piao, S.L., Peylin, P., 2010. Benchmarking coupled climate-carbon models against long-term atmospheric CO₂ measurements. *Global Biogeochem. Cy.* 24, 2. <https://doi.org/10.1029/2009gb003556>.
- Cao, R., Huang, H., Wu, G., Han, D., Jiang, Z., Di, K., Hu, Z., 2022. Spatiotemporal variations in the ratio of transpiration to evapotranspiration and its controlling factors across terrestrial biomes. *Agric. for. Meteorol* 321, 108984. <https://doi.org/10.1016/j.agrformet.2022.108984>.
- Chen, F., Mitchell, K., Schaake, J., Xue, Y., Pan, H.L., Koren, V., Duan, Q.Y., Ek, M., Betts, A., 1996. Modeling of land surface evaporation by four schemes and comparison with FIFE observations. *J. Geophys. Res.-Atmos.* 101, 7251–7268. <https://doi.org/10.1029/95jd02165>.
- Chen, C., Park, T., Wang, X., Piao, S., Xu, B., Chaturvedi, R.K., Fuchs, R., Brovkin, V., Ciais, P., Fensholt, R., Tømmervik, H., Bala, G., Zhu, Z., Nemani, R.R., Myneni, R.B., 2019. China and India lead in greening of the world through land-use management. *Nat. Sustain.* 2, 122–129. <https://doi.org/10.1038/s41893-019-0220-7>.
- Dickinson, R.E., Shaikh, M., Bryant, R., Graumlich, L., 1998. Interactive Canopies for a Climate Model. *Journal of Climate* (pp. 2823-2836). Boston MA, USA: American Meteorological Society.
- Dickinson, R.E., 1984. Modeling evapotranspiration for three-dimensional global climate models. *Climate processes and climate sensitivity* (pp. 58-72).
- Duursma, R.A., Payton, P., Bange, M.P., Broughton, K.J., Smith, R.A., Medlyn, B.E., Tissue, D.T., 2013. Near-optimal response of instantaneous transpiration efficiency to vapour pressure deficit, temperature and [CO₂] in cotton (*Gossypium hirsutum* L.). *Agric. for. Meteorol* 168, 168–176. <https://doi.org/10.1016/j.agrformet.2012.09.005>.
- Fang, S., Zhao, C., Jie, S., Yu, K., 2013. Canopy interception of *Pinus tabulaeformis* plantation on Longzhong Loess Plateau, Northwest China: characteristics and simulation (in Chinese). *J. Appl. Ecol.* 24, 1509–1516. <https://doi.org/10.13287/j.1001-9332.2013.0326>.
- Fisher, J.B., Tu, K.P., Baldocchi, D.D., 2008. Global estimates of the land-atmosphere water flux based on monthly AVHRR and ISLSCP-II data, validated at 16 FLUXNET sites. *Remote Sens. Environ.* 112, 901–919. <https://doi.org/10.1016/j.rse.2007.06.025>.
- Ge, Z.-M., Zhou, X., Kellomäki, S., Peltola, H., Wang, K.-Y., 2011. Climate, canopy conductance and leaf area development controls on evapotranspiration in a boreal coniferous forest over a 10-year period: a united model assessment. *Ecol. Model.* 222, 1626–1638. <https://doi.org/10.1016/j.ecolmodel.2011.02.022>.
- Good, S.P., Noone, D., Bowen, G., 2015. Hydrologic connectivity constrains partitioning of global terrestrial water fluxes. *Science* 349, 175–177. <https://doi.org/10.1126/science.aaa5931>.
- Good, S.P., Moore, G.W., Miralles, D.G., 2017. A mesic maximum in biological water use demarcates biome sensitivity to aridity shifts. *Nat. Ecol. Evol.* 1, 1883–1888. <https://doi.org/10.1038/s41559-017-0371-8>.
- Haddeland, I., Lettenmaier, D.P., Skaugen, T., 2006. Reconciling simulated moisture fluxes resulting from alternate hydrologic model time steps and energy budget closure assumptions. *J. Hydrometeorol.* 7, 355–370. <https://doi.org/10.1175/JHM496.1>.
- Hosseini, A., Mocko, D.M., Brunzell, N.A., Kumar, S.V., Mahanama, S., Arsenault, K., Roundy, J.K., 2022. Understanding the impact of vegetation dynamics on the water cycle in the Noah-MP model. *Front. Water* 4, 925852. <https://doi.org/10.3389/frwa.2022.925852>.
- Jasechko, S., Sharp, Z.D., Gibson, J.J., Birks, S.J., Yi, Y., Fawcett, P.J., 2013. Terrestrial water fluxes dominated by transpiration. *Nature* 496, 347–350. <https://doi.org/10.1038/nature11983>.
- Jia, K., Liang, S., Gu, X., Baret, F., Wei, X., Wang, X., Yao, Y., Yang, L., Li, Y., 2016. Fractional vegetation cover estimation algorithm for Chinese GF-1 wide field view data. *Remote Sens. Environ.* 177, 184–191. <https://doi.org/10.1016/j.rse.2016.02.019>.
- Jia, K., Liang, S., Wei, X., Yao, Y., Yang, L., Zhang, X., Liu, D., 2018. Validation of Global Land Surface Satellite (GLASS) fractional vegetation cover product from MODIS data in an agricultural region. *Remote Sens. Lett.* 9, 847–856. <https://doi.org/10.1080/2150704X.2018.1484958>.
- Jiang, F., Xie, X., Liang, S., Wang, Y., Zhu, B., Zhang, X., Chen, Y., 2021. Loess Plateau evapotranspiration intensified by land surface radiative forcing associated with ecological restoration. *Agric. for. Meteorol* 311, 108669. <https://doi.org/10.1016/j.agrformet.2021.108669>.
- Jiang, F., Xie, X., Wang, Y., Liang, S., Zhu, B., Meng, S., Zhang, X., Chen, Y., Liu, Y., 2022. Vegetation greening intensified transpiration but constrained soil evaporation on the Loess Plateau. *J. Hydrol* 614, 128514. <https://doi.org/10.1016/j.jhydrol.2022.128514>.
- Jiao, L., Lu, N., Sun, G., Ward, E.J., Fu, B., 2015. Biophysical controls on canopy transpiration in a black locust (*Robinia pseudoacacia*) plantation on the semi-arid Loess Plateau, China. *Ecohydrology* 9, 1068–1081. <https://doi.org/10.1002/eco.1711>.
- Jiao, L., Lu, N., Fu, B., Wang, J., Li, Z., Fang, W., Liu, J., Wang, C., Zhang, L., 2018. Evapotranspiration partitioning and its implications for plant water use strategy: evidence from a black locust plantation in the semi-arid Loess Plateau China. *Forest Ecol. Manag.* 424, 428–438. <https://doi.org/10.1016/j.foreco.2018.05.011>.
- Jung, M., Koiraal, S., Weber, U., Ichii, K., Gans, F., Camps-Valls, G., Papale, D., Schwalm, C., Tramontana, G., Reichstein, M., 2019. The FLUXCOM ensemble of global land-atmosphere energy fluxes. *Sci. Data* 6, 128514. <https://doi.org/10.1038/s41597-019-0076-8>.
- Lawrence, D.M., Thornton, P.E., Oleson, K.W., Bonan, G.B., 2007. The Partitioning of evapotranspiration into transpiration, soil evaporation, and canopy evaporation in a GCM: impacts on land-atmosphere interaction. *J. Hydrometeorol.* 8, 862–880. <https://doi.org/10.1175/jhm596.1>.
- Lawrence, D.M., Fisher, R.A., Koven, C.D., Oleson, K.W., Swenson, S.C., Bonan, G., Collier, N., Ghimire, B., van Kampenhout, L., Kennedy, D., Kluzek, E., Lawrence, P.J., Li, F., Li, H., Lombardozzi, D., Riley, W.J., Sacks, W.J., Shi, M., Vertenstein, M., Wieder, W.R., Xu, C., Ali, A.A., Badger, A.M., Bish, G., van den Broeke, M., Brunke, M.A., Burns, S.P., Buzan, J., Clark, M., Craig, A., Dahlin, K., Drewniak, B., Fisher, J.B., Flanner, M., Fox, A.M., Gentile, P., Hoffman, F., Keppel-Aleks, G., Knox, R., Kumar, S., Lenaerts, J., Leung, L.R., Lipscomb, W.H., Lu, Y., Pandey, A., Pelletier, J.D., Perket, J., Randerson, J.T., Ricciuto, D.M., Sanderson, B.M., Slater, A., Subin, Z.M., Tang, J., Thomas, R.Q., Val Martin, M., Zeng, X., 2019. The community land model version 5: description of new features, benchmarking, and impact of forcing uncertainty. *J. Adv. Model. Earth Sy.* 11, 4245–4287. <https://doi.org/10.1029/2018ms001583>.
- Leng, G., Tang, Q., Rayburg, S., 2015. Climate change impacts on meteorological, agricultural and hydrological droughts in China. *Global Planet. Change* 126, 23–34. <https://doi.org/10.1016/j.gloplacha.2015.01.003>.
- Li, L., Song, X., Xia, L., Fu, N., Feng, D., Li, H., Li, Y., 2020. Modelling the effects of climate change on transpiration and evaporation in natural and constructed grasslands in the semi-arid Loess Plateau China. *Agr. Ecosyst. Environ.* 302, 107077. <https://doi.org/10.1016/j.agee.2020.107077>.
- Lian, X., Piao, S., Huntingford, C., Li, Y., Zeng, Z., Wang, X., Ciais, P., McVicar, T.R., Peng, S., Otlé, C., Yang, H., Yang, Y., Zhang, Y., Wang, T., 2018. Partitioning global land evapotranspiration using CMIP5 models constrained by observations. *Nat. Clim. Change* 8, 640–646. <https://doi.org/10.1038/s41558-018-0207-9>.
- Liang, S., Cheng, J., Jia, K., Jiang, B., Liu, Q., Xiao, Z., Yao, Y., Yuan, W., Zhang, X., Zhao, X., Zhou, J., 2021. The global land surface satellite (GLASS) product suite. *Bull. Am. Meteorol. Soc.* 102, E323–E337. <https://doi.org/10.1175/bams-d-18-0341.1>.
- Liang, X., Lettenmaier, D.P., Wood, E.F., Burges, S.J., 1994. A simple hydrologically based model of land surface water and energy fluxes for general circulation models. *J. Geophys. Res.-Atmos.* 99, 14415–14428. <https://doi.org/10.1029/94JD00483>.
- Liu, Y., Kumar, M., Katul, G.G., Feng, X., Konings, A.G., 2020. Plant hydraulics accentuates the effect of atmospheric moisture stress on transpiration. *Nat. Clim. Change* 10, 691–695. <https://doi.org/10.1038/s41558-020-0781-5>.
- Liu, Z., Wang, Y., Tian, A., Liu, Y., Webb, A.A., Wang, Y., Zuo, H., Yu, P., Xiong, W., Xu, L., 2017. Characteristics of canopy interception and its simulation with a revised Gash model for a larch plantation in the Liupan Mountains. *China. J. Forestry Res.* 29, 187–198. <https://doi.org/10.1007/s11676-017-0407-6>.
- Liu, Y., Xie, X., Tursun, A., Wang, Y., Jiang, F., Zheng, B., 2023. Surface water expansion due to increasing water demand on the Loess Plateau. *J. Hydrol.- Reg. Stud.* 49, 101485. <https://doi.org/10.1016/j.ejrh.2023.101485>.
- Liu, J., 2008. A study on the Hillslope ecohydrological processes and vegetation carrying capacity in the small catchment of Diedieoug, Liupanshan Mountain (in Chinese). In: Chinese Academy Forestry.
- Long, D., Longuevergne, L., Scanlon, B.R., 2014. Uncertainty in evapotranspiration from land surface modeling, remote sensing, and GRACE satellites. *Water Resour. Res.* 50, 1131–1151. <https://doi.org/10.1002/2013wr014581>.
- Louis, J.-F., 1979. A parametric model of vertical eddy fluxes in the atmosphere. *Bound.-Lay. Meteorol.* 17, 187–202. <https://doi.org/10.1007/BF00117978>.
- Luo, X., Liang, X., Lin, J.S., 2016. Plant transpiration and groundwater dynamics in water-limited climates: Impacts of hydraulic redistribution. *Water Resour. Res.* 52, 4416–4437. <https://doi.org/10.1002/2015wr017316>.
- Ma, H., Liang, S., 2022. Development of the GLASS 2530-m leaf area index product (version 6) from MODIS data using the bidirectional LSTM deep learning model. *Remote Sens. Environ.* 273, 112985. <https://doi.org/10.1016/j.rse.2022.112985>.
- Meinzer, F.C., Evolution, 1993. Stomatal control of transpiration, 8, 289–294. doi: 10.1016/0169-5347(93)90257-P.
- Meng, S., Xie, X., Liang, S., 2017. Assimilation of soil moisture and streamflow observations to improve flood forecasting with considering runoff routing lags. *J. Hydrol* 550, 568–579. <https://doi.org/10.1016/j.jhydrol.2017.05.024>.
- Meng, S., Xie, X., Zhu, B., Wang, Y., 2020. The relative contribution of vegetation greening to the hydrological cycle in the Three-North region of China: a modelling analysis. *J. Hydrol* 591, 125689. <https://doi.org/10.1016/j.jhydrol.2020.125689>.
- Mianabadi, A., Coenders-Gerrits, M., Shirazi, P., Gahraman, B., Alizadeh, A., 2019. A global Budyko model to partition evaporation into interception and transpiration. *Hydrol. Earth Syst. Sci.* 23, 4983–5000. <https://doi.org/10.5194/hess-23-4983-2019>.
- Miralles, D.G., Jiménez, C., Jung, M., Michel, D., Ershadi, A., McCabe, M.F., Hirschi, M., Martens, B., Dolman, A.J., Fisher, J.B., Mu, Q., Seneviratne, S.I., Wood, E.F., Fernández-Prieto, D., 2016. The WACMOS-ET project – part 2: evaluation of global terrestrial evaporation data sets. *Hydrol. Earth Syst. Sci.* 20, 823–842. <https://doi.org/10.5194/hess-20-823-2016>.

- Monteith, J.L., Unsworth, M.H., Webb, A., 1994. Principles of environmental physics. *Q. J. Roy. Meteor. Soc.* 120, 1699.
- Mu, Q., Heinsch, F.A., Zhao, M., Running, S.W., 2007. Development of a global evapotranspiration algorithm based on MODIS and global meteorology data. *Remote Sens. Environ.* 111, 519–536. <https://doi.org/10.1016/j.rse.2007.04.015>.
- Nijssen, B., Schnur, R., Lettenmaier, D.P., 2001. Global retrospective estimation of soil moisture using the variable infiltration capacity land surface model, 1980–93. *J. Climate* 14, 1790–1808. [https://doi.org/10.1175/1520-0442\(2001\)014<1790:GREOSM>2.0.CO;2](https://doi.org/10.1175/1520-0442(2001)014<1790:GREOSM>2.0.CO;2).
- Oleson, K., Dai, Y., Bonan, G., Rosilovich, M., Dickinson, R., Dirmeyer, P., Hoffman, F., Houser, P., Levis, S., Niu, G., 2004. Technical description of the Community Land Model (CLM). NCAR Tech. Note. In: NCAR/TN-461+ STR, 173pp.
- Paschalis, A., Faticchi, S., Pappas, C., Or, D., 2018. Covariation of vegetation and climate constrains present and future T/ET variability. *Environ. Res. Lett.* 13 <https://doi.org/10.1088/1748-9326/aae267>.
- Piao, S., Wang, X., Park, T., Chen, C., Lian, X., He, Y., Bjerke, J.W., Chen, A., Ciais, P., Tommervik, H., Nemani, R.R., Myneni, R.B., 2020. Characteristics, drivers and feedbacks of global greening. *Nat. Rev. Earth Env.* 1, 14–27. <https://doi.org/10.1038/s43017-019-0001-x>.
- Sankarasubramanian, A., Vogel, R.M., Limbrunner, J.F., 2001. Climate elasticity of streamflow in the United States. *Water Resour. Res.* 37, 1771–1781. <https://doi.org/10.1029/2000wr900330>.
- Sato, H., Ito, A., Ito, A., Ise, T., Kato, E., 2014. Current status and future of land surface models. *Soil Sci. Plant Nutr.* 61, 34–47. <https://doi.org/10.1080/00380768.2014.917593>.
- Schlesinger, W.H., Jasechko, S., 2014. Transpiration in the global water cycle. *Agric. for. Meteorol.* 189–190, 115–117. <https://doi.org/10.1016/j.agrformet.2014.01.011>.
- Shu, Z., Zhang, B., Tian, L., Zhao, X., 2022. Improving dynamic vegetation modeling in noah-MP by parameter optimization and data assimilation over China's Loess Plateau. *J. Geophys. Res.-Atmos.* 127, e2022JD036703 <https://doi.org/10.1029/2022jd036703>.
- Sitch, S., Friedlingstein, P., Gruber, N., Jones, S.D., Murray-Tortarolo, G., Ahlström, A., Doney, S.C., Graven, H., Heinze, C., Huntingford, C., Levis, S., Levy, P.E., Lomas, M., Poulter, B., Viovy, N., Zaehle, S., Zeng, N., Arneth, A., Bonan, G., Bopp, L., Canadell, J.G., Chevallier, F., Ciais, P., Ellis, R., Gloor, M., Peylin, P., Piao, S.L., Le Quéré, C., Smith, B., Zhu, Z., Myneni, R., 2015. Recent trends and drivers of regional sources and sinks of carbon dioxide. *Biogeosciences* 12, 653–679. <https://doi.org/10.5194/bg-12-653-2015>.
- Song, L., Liu, S., Kustas, W.P., Nieto, H., Sun, L., Xu, Z., Skaggs, T.H., Yang, Y., Ma, M., Xu, T., Tang, X., Li, Q., 2018. Monitoring and validating spatially and temporally continuous daily evaporation and transpiration at river basin scale. *Remote Sens. Environ.* 219, 72–88. <https://doi.org/10.1016/j.rse.2018.10.002>.
- Sus, O., Poyatos, R., Barba, J., Carvalhais, N., Llorens, P., Williams, M., Vilalta, J.M., 2014. Time variable hydraulic parameters improve the performance of a mechanistic stand transpiration model. a case study of Mediterranean Scots pine sap flow data assimilation. *Agric. for. Meteorol.* 198–199, 168–180. <https://doi.org/10.1016/j.agrformet.2014.08.009>.
- Talsma, C.J., Good, S.P., Jimenez, C., Martens, B., Fisher, J.B., Miralles, D.G., McCabe, M. F., Purdy, A.J., 2018a. Partitioning of evapotranspiration in remote sensing-based models. *Agric. For. Meteorol.* 260–261, 131–143. <https://doi.org/10.1016/j.agrformet.2018.05.010>.
- Talsma, C.J., Good, S.P., Miralles, D.G., Fisher, J.B., Martens, B., Jimenez, C., Purdy, A.J., 2018b. Sensitivity of evapotranspiration components in remote sensing-based models. *Remote Sens.* 10, 1601. <https://doi.org/10.3390/rs10101601>.
- Tian, F., Qiu, G., Yang, Y., Lü, Y., Xiong, Y., 2013. Estimation of evapotranspiration and its partition based on an extended three-temperature model and MODIS products. *J. Hydrol.* 498, 210–220. <https://doi.org/10.1016/j.jhydrol.2013.06.038>.
- Tian, J., 2005. Studies on Water Consumption Characteristics of Main Tree Species of Soil And Water Conservation Forest In Semi-Arid Region On the Loess Plateau (in Chinese). In: Beijing Forestry University.
- Wang, L., Good, S.P., Caylor, K.K., 2014. Global synthesis of vegetation control on evapotranspiration partitioning. *Geophys. Res. Lett.* 41, 6753–6757. <https://doi.org/10.1002/2014gl061439>.
- Wang, Y., Wang, X., Gao, X., Li, Z., 2017. Canopy precipitation redistribution of typical forest vegetation in Baichazigou Watershed, Daqing Mountains of Inner Mongolia (in Chinese). *Journal of Inner Mongolia Forestry Science and Technology* 43, 6–9.
- Wei, Z., Yoshimura, K., Wang, L., Miralles, D.G., Jasechko, S., Lee, X., 2017. Revisiting the contribution of transpiration to global terrestrial evapotranspiration. *Geophys. Res. Lett.* 44, 2792–2801. <https://doi.org/10.1002/2016gl072235>.
- Xiao, Z., Liang, S., Wang, J., Chen, P., Yin, X., Zhang, L., Song, J., 2014. Use of general regression neural networks for generating the GLASS Leaf area index product from time-Series MODIS surface reflectance. *IEEE Trans. Geosci. Remote Sens.* 52, 209–223. <https://doi.org/10.1109/tgrs.2013.2237780>.
- Xiao, Z., Liang, S., Wang, J., Xiang, Y., Zhao, X., Song, J., 2016. Long-time-series global land surface satellite leaf area index product derived from MODIS and AVHRR surface reflectance. *IEEE Trans. Geosci. Remote Sens.* 54, 5301–5318. <https://doi.org/10.1109/tgrs.2016.2560522>.
- Xie, X., Liang, S., Yao, Y., Jia, K., Meng, S., Li, J., 2015. Detection and attribution of changes in hydrological cycle over the Three-North region of China: climate change versus afforestation effect. *Agric. for. Meteorol.* 203, 74–87. <https://doi.org/10.1016/j.agrformet.2015.01.003>.
- Yang, Z., Bai, P., Li, Y., 2022. Quantifying the effect of vegetation greening on evapotranspiration and its components on the Loess Plateau. *J. Hydrol.* 613 <https://doi.org/10.1016/j.jhydrol.2022.128446>.
- Yang, Y., Guan, K., Peng, B., Pan, M., Franz, T.E., 2021. High-resolution spatially explicit land surface model calibration using field-scale satellite-based daily evapotranspiration product. *J. Hydrol.* 596, 125730. <https://doi.org/10.1016/j.jhydrol.2020.125730>.
- Yang, L., Jia, K., Liang, S., Liu, J., Wang, X., 2016. Comparison of four machine learning methods for generating the GLASS fractional vegetation cover product from MODIS data. *Remote Sens.* 8, 682. <https://doi.org/10.3390/rs8080682>.
- Yang, Y., Roderick, M.L., Guo, H., Miralles, D.G., Zhang, L., Faticchi, S., Luo, X., Zhang, Y., McVicar, T.R., Tu, Z., Keenan, T.F., Fisher, J.B., Gan, R., Zhang, X., Piao, S., Zhang, B., Yang, D., 2023. Evapotranspiration on a greening earth. *Nat. Rev. Earth Env.* 4, 626–641. <https://doi.org/10.1038/s43017-023-00464-3>.
- Yeh, P., Weedon, G.P., Viterbo, P., Stacke, T., Polcher, J., Oki, T., Koirala, S., Kabat, P., Heinke, J., Harding, R., Hanasaki, N., Hagemann, S., Gosling, S.N., Gomes, S., Gerten, D., Folwell, S., Best, M., Bertrand, N., Arnell, N.W., Voß, F., Ludwig, F., Franssen, W., Clark, D.B., Haddeland, I., 2011. Multimodel estimate of the global terrestrial water balance: setup and first results. *J. Hydrometeorol.* 12, 869–884. <https://doi.org/10.1175/2011jhm1324.1>.
- Zhang, Y.Q., Chiew, F.H.S., Zhang, L., Leuning, R., Cleugh, H.A., 2008. Estimating catchment evaporation and runoff using MODIS leaf area index and the Penman-Monteith equation. *Water Resour. Res.* 44, W10420. <https://doi.org/10.1029/2007wr006563>.
- Zhang, Y., Chiew, F.H.S., Peña-Arancibia, J., Sun, F., Li, H., Leuning, R., 2017. Global variation of transpiration and soil evaporation and the role of their major climate drivers. *J. Geophys. Res.-Atmos.* 122, 6868–6881. <https://doi.org/10.1002/2017jd027025>.
- Zhang, Y., Kong, D., Gan, R., Chiew, F.H.S., McVicar, T.R., Zhang, Q., Yang, Y., 2019. Coupled estimation of 500 m and 8-day resolution global evapotranspiration and gross primary production in 2002–2017. *Remote Sens. Environ.* 222, 165–182. <https://doi.org/10.1016/j.rse.2018.12.031>.
- Zhang, B., Tian, L., Yang, Y., He, X., 2022. Revegetation does not decrease water yield in the Loess Plateau of China. *Geophys. Res. Lett.* 49, e2022GL098025 <https://doi.org/10.1029/2022gl098025>.
- Zhang, Y., Yuan, C., Chen, N., Levia, D.F., 2023. Rainfall partitioning by vegetation in China: a quantitative synthesis. *J. Hydrol.* 617, 128946. <https://doi.org/10.1016/j.jhydrol.2022.128946>.
- Zhou, S., Yu, B., Zhang, Y., Huang, Y., Wang, G., 2016. Partitioning evapotranspiration based on the concept of underlying water use efficiency. *Water Resour. Res.* 52, 1160–1175. <https://doi.org/10.1002/2015wr017766>.